OPEN

Weak Anti-localization and Quantum Oscillations of Surface States in Topological Insulator Bi$_2$Se$_2$Te

Lihong Bao[1]*, Liang He[2]*, Nicholas Meyer[1], Xufeng Kou[2], Peng Zhang[3], Zhi-gang Chen[4], Alexei V. Fedorov[3], Jin Zou[4], Trevor M. Riedemann[5], Thomas A. Lograsso[5], Kang L. Wang[2], Gary Tuttle[1] & Faxian Xiu[1]

[1]Department of Electrical and Computer Engineering, Iowa State University, Ames, IA 50011, USA, [2]Department of Electrical Engineering, University of California, Los Angeles, CA 90095, USA, [3]Advanced Light Source Division, Lawrence Berkeley National Laboratory, Berkeley, CA 94720, USA, [4]Materials Engineering and Center for Microscopy and Microanalysis, The University of Queensland, Brisbane QLD 4072, Australia, [5]The Ames Laboratory, Ames, IA 50011, USA.

Topological insulators, a new quantum state of matter, create exciting opportunities for studying topological quantum physics and for exploring spintronic applications due to their gapless helical metallic surface states. Here, we report the observation of weak anti-localization and quantum oscillations originated from surface states in Bi$_2$Se$_2$Te crystals. Angle-resolved photoemission spectroscopy measurements on cleaved Bi$_2$Se$_2$Te crystals show a well-defined linear dispersion without intersection of the conduction band. The measured weak anti-localization effect agrees well with the Hikami-Larkin-Nagaoka model and the extracted phase coherent length shows a power-law dependence with temperature ($l_\phi \sim T^{-0.44}$), indicating the presence of the surface states. More importantly, the analysis of a Landau-level fan diagram of Shubnikov-de Hass oscillations yields a finite Berry phase of $\sim 0.42\pi$, suggesting the Dirac nature of the surface states. Our results demonstrate that Bi$_2$Se$_2$Te can serve as a suitable topological insulator candidate for achieving intrinsic quantum transport of surface Dirac fermions.

As a new class of quantum matter, topological insulators (TIs) with time-reversal-symmetry protected helical surface states[1-4] induced by a strong spin-orbit coupling[5-7] have been identified as promising materials for exploiting exciting physics such as Majorana fermions[8], monopole magnets[9], and a super-conducting proximity effect[8,10], as well as developing potential applications in quantum computing[11]. Bi-based chalcogenides are confirmed as prototypical TIs due to their simple surface Dirac cone and relatively large bulk energy gap[7]. To probe the exotic spin-locked Dirac fermions and control the helical surface states, substantial effort has been made in both improving material performance by electrostatic gating[12-15], substitutional doping[16-20], and stoichiometric component engineering[21-24] in ternary tetradymite compounds[25], and in developing sensitive techniques for revealing surface helical features, such as angle-resolved photoemission spectroscopy (ARPES)[26-30], scanning tunneling microscopy[31-33], low-temperature transport[12,19,34-36], and optical polarization[37]. However, the dominant bulk conduction arising from naturally occurring crystal imperfections and residual carrier doping has greatly hindered the detection of Dirac fermions by means of weak anti-localization effect[13] and quantum oscillations[34] at low temperatures. Recently, Bi$_2$Te$_2$Se (BTS), with a ternary tetradymite structure, has shown a low carrier concentration of $\sim 10^{16}$ cm^{-3} and a large bulk resistivity of ~ 6 Ω cm due to the ordered occupation of Te/Se in the quintuple-layer unit[14,38]. In contrast, Bi$_2$Se$_2$Te (BST) has rarely been investigated although theoretical calculations predict that both BTS and BST with ordered or partially disordered atomic structures are stable topological insulators[25].

In this work, we report weak anti-localization (WAL) and Shubnikov-de Haas (SdH) oscillations originating from the BST surface states. The WAL effect is only sensitive to the perpendicular component of the magnetic field and can be well described by the Hikami-Larkin-Nagaoka model where the temperature dependence of the phase coherent length shows a power-law behavior of $\sim T^{-0.44}$. SdH oscillations also reveal a well defined 2D Fermi surface in the BST crystal which survives up to ~ 7 K. The finite Berry phase of 0.42π extracted from the SdH oscillations elucidates the Dirac nature of surface states. More importantly, the surface conductance contributes up to $\sim 57\%$ of the total conductance, indicative of dominant surface transport.
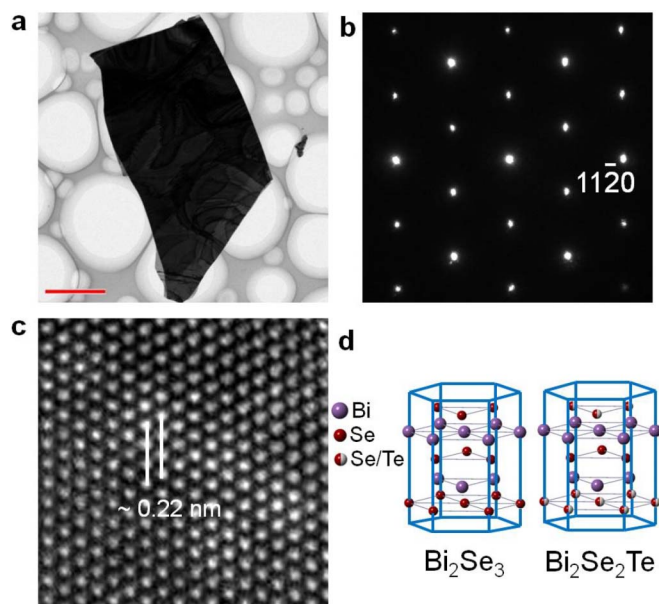
Figure 1 | Structural characterization of cleaved flakes from Bi_2Se_2Te (BST) crystal. (a) Low-magnification TEM image, (b) Selected area electron diffraction pattern, (c) High-resolution TEM (HRTEM) image of a BST flake on a holey carbon grid, respectively. The sharp SAED pattern in (b) indicates the high-quality single crystal. The HRTEM image in (c) reveals a perfect crystalline structure and the spacing between the ($11\bar{2}0$) atomic planes is resolved to be 0.22 nm (marked by a pair of parallel lines). (d) Layered crystal structure of Bi_2Se_3 and Bi_2Se_2Te, showing the disordered occupation of Se/Te atoms in outer quintuple layers. Scale bars in (a) is 2 μm.

Results

Structural characterizations of BST crystal. A high-quality single crystal of BST with a small concentration gradient was produced via the Bridgman technique. Elemental concentration profiles along the ingot were obtained by using wavelength dispersive micro-analysis. The results show that the compositions of Bi, Se, and Te in the crystal

have a small variation along the growth direction of the ingot (less than 3%), confirming the high quality (Supplementary Fig. S1). Transmission electron microscopy (TEM) was performed to determine the structural characteristics. Flakes of the BST were obtained by mechanical exfoliation of cleaved crystals. A low magnification TEM image is shown in Fig. 1a, revealing sizes of several to tens micrometers in width/length for the exfoliated flakes. Sharp selected-area electron diffraction pattern indicated a perfect single crystalline rhombohedral phase of BST (Fig. 1b). The atomic plane spacings in high-resolution TEM images were determined to be 0.22 nm, as marked by a pair of parallel lines in Fig. 1c, which is consistent with the d-spacings of the ($11\bar{2}0$) planes in BST (Supplementary Table S1). The powder X-ray diffraction (XRD) pattern shows deviations from that of ordered skippenite structure (Supplementary Fig. S2)[39], which may suggest a disordered occupation of Te/Se on outer quintuple layers[25] (Fig. 1d). Unlike the central-layer substitution in BTS[14,40], the partially disordered BST structure resulting from random Te substitutions of Se atoms in outer quintuple layers is a very low-energy structure and thus conforms to Hume-Rothery solid-solution rules[25]. Furthermore, the powder XRD refinement experiments confirm such a disordered occupation of Te/Se on the outermost quintuple layers and present the non-stoichiometric formula of $Bi_2Se_{1.88}Te_{1.12}$ for our BST crystal (Supplementary Table S1). This is in a good agreement with previous XRD experiments on a solid solution of $Bi_2Te_{3-x}Se_x$[41]. In fact, the carrier concentration in $Bi_2Te_{3-x}Se_x$ is extremely sensitive to the value of x. The non-stoichiometric BST with a low x can greatly reduce the residual carrier concentration in the bulk[40] and thus benefits the surface-dominated transport, as to be discussed later.

Electronic structure of BST crystal. To verify the characteristics of the surface states of the BST crystal, high–resolution ARPES experiments were performed under different photon energies. Fig. 2a shows the ARPES intensity around the center of the surface Brillouin zone. A familiar "V" shaped surface state with linear dispersion was clearly resolved, indicating the presence of Dirac fermions. The Fermi level is located ~0.3 eV above the Dirac point, which is lower than the reported value of 0.425 eV[42], probably because of the reduced carrier density in the bulk giving
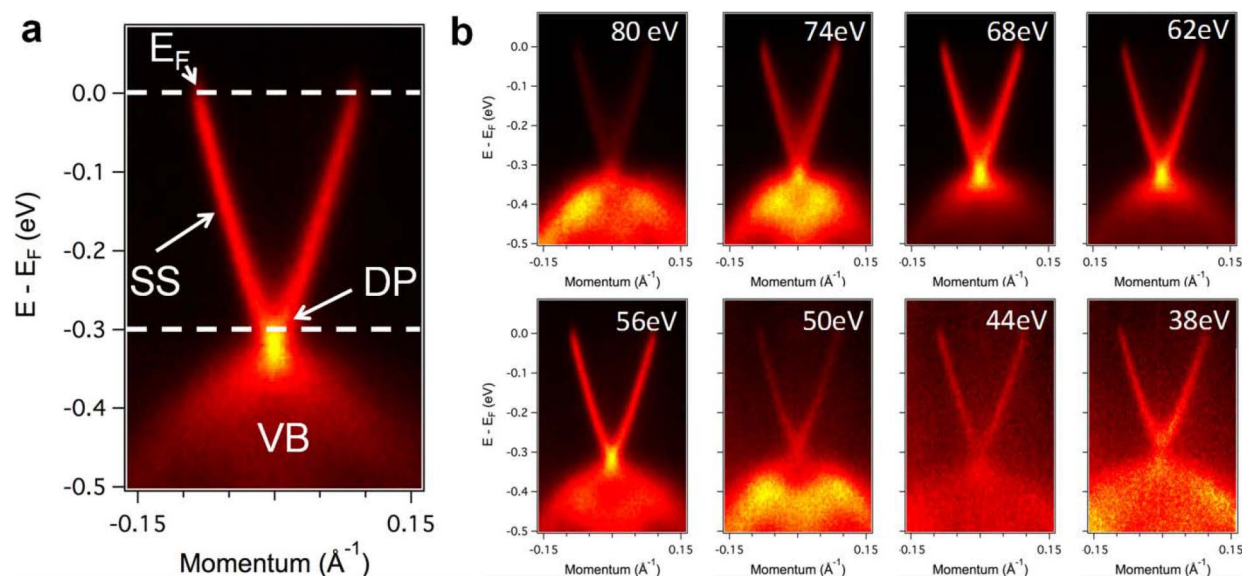

Figure 2 | Angle-resolved photoemission spectroscopy (ARPES) of Bi_2Se_2Te (BST) crystal. (a) Measured band structure curve of BST along the Γ point taken at a photon energy of 60 eV. A single Dirac cone was clearly resolved and no conduction band was observed. The Dirac point (DP) is located ~0.3 eV away from the Fermi level. (b) Photo-energy-dependent band structure curves of BST at different excitation photon energies of 80, 74, 68, 62, 56, 50, 46, and 38 eV, respectively.

rise to a lower position of Fermi level relative to the Dirac point (Fig. 2a). Furthermore, the ARPES measurements under a series of photon excitation energies show that the Fermi level intersects only the Dirac cone with an absence of the conduction band in the band structure (Fig. 2b), which is favorable in the course of searching for an ideal TI candidate[24,40,43]. It is also revealed that the "V" shaped dispersion of surface states is stationary with varied photon energy unlike the "M" shaped dispersion of the VB (Fig. 2b), showing the robustness of the surface states with photon energy[24]. The Dirac cone intersects the Fermi level at a momentum of 0.07 Å^{-1}, yielding a Fermi velocity of 6.4×10^5 m/s by momentum distribution curve fitting (Supplementary Fig. S3), which is reasonably close to the reported value[42].

Temperature-dependent longitudinal and Hall resistances of BST crystal. Hall bar devices with standard six-terminal geometry were fabricated for transport measurements. The temperature dependence of the longitudinal resistance of the BST crystal is shown in Fig. 3a. The longitudinal resistance R_{xx} increases roughly two orders of magnitude upon cooling from room temperature, indicating a non-metallic behavior[14,38,40,43]. The Arrhenius plot of R_{xx} (lower inset of Fig. 3a) exhibits thermal activation behavior in a temperature range from 300 K down to 120 K. By using $R_{xx} \sim e^{E_a/k_B T}$, where E_a is the activation energy and k_B is the Boltzmann constant, an activation energy of about 100 meV is extracted. This value is four times larger than the 23 meV of BTS[14] but remains the same order of magnitude to that of Sn-doped BTS[20]. A reasonable fit to the three-dimensional (3D) variable-range hopping model (VRH, $G_{xx} \sim \exp[-(T/T_0)^{-1/4}]$[14,44,45], suggests that the transport property is dominated by 3D VRH behavior from 100 to 20 K (red solid line in Fig. 3b), while the deviation from the fit at low temperatures ($<$ 20 K) signifies a parallel metallic conduction from the surface states, although no apparent saturation was observed for R_{xx} at low temperatures (upper inset of Fig. 3a). This behavior can be further supported by the observation of the weak anti-localization effect and Shubnikov-de Hass (SdH) oscillations (discussed later). The temperature-dependent low-field (near B = 0 T) Hall coefficient (Fig. 3c) R_H shows a sign transition from positive to negative upon cooling from 300 to 1.9 K, representing a charge carrier switch from holes to electrons in the BST crystal similar to previously reported results in the BTS system[14,40]. The inset in Fig. 3c displays magnetic field-dependent Hall resistance at 1.9 K, showing little difference of R_H between low-fields and high-fields. Above $\sim$100 K, the Hall coefficient R_H has a thermal activation behavior, suggesting that the Fermi level is far from the conduction band and is located inside the bulk band gap[20]. The low-field R_H of -10.9 Ω T^{-1} at 1.9 K provides an estimated electron concentration of 1.4×10^{16} cm^{-3}, in the same order of magnitude as that of BTS[14,40]. The Hall mobility can be determined to be 264 cm^{2}V^{-1}s^{-1}. It is believed that the low mobility of bulk carriers may enhance the surface state contribution due to the suppression of bulk carrier interference with quantum oscillations[14,22,40]. In our case, such a low carrier concentration and bulk carrier mobility may help to detect the surface transport in the BST crystal.

Weak anti-localization (WAL) effect in BST crystal. As a quantum correction to classical magnetoresistance, the WAL effect is a signature of topological surface states originating from the Berry's phase which is associated with the helical states[13,15,46]. The sheet magnetoresistance at different tilt angles (θ) reveals the features of the WAL effect - the presence of sharp cusps at zero magnetic field[13,18,22,47–49] (Supplementary Fig. S4a). However, the existence of cusp features of magnetoresistance at $\theta = 0$ gives a hint to a partial 3D contribution of bulk spin-orbit coupling, which was also observed in Bi$_2$(Se$_x$Te$_{1-x}$)$_3$ nanoribbons (Supplementary Fig. S4a)[22]. The WAL induced by 2D surface states is characterized by a sole dependence on
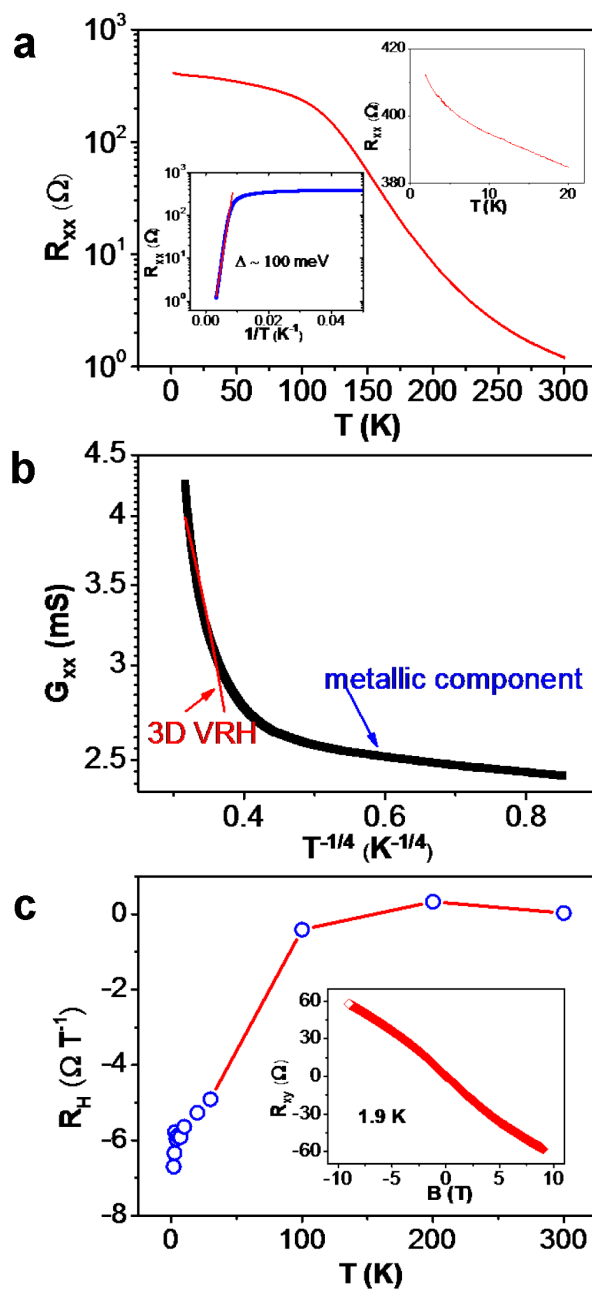

Figure 3 | Electrical transport of Bi$_2$Se$_2$Te (BST) crystal under zero magnetic field. (a) Temperature-dependence of longitudinal resistance R_{xx}. Lower inset shows the Arrhenius plot of $R_{xx} \sim e^{E_a/k_B T}$, which yields an activation energy of 100 meV in the temperature range of 120-300 K. Upper inset plots the R_{xx} at temperature lower than 20 K and no apparent saturation was observed. (b) A plot of longitudinal conductance G_{xx} vs $T^{-1/4}$. Solid line (red) is the data fit to the 3D variable range hopping (VRH): $G_{xx} \sim \exp[-(T/T_0)^{-1/4}]$; deviation from the fit at low temperature signifies the parallel metallic conduction. (c) Temperature-dependence of the low-field R_H. Inset shows the R_{xy} curve at 1.9 K. The dominant charge carriers are electrons.

the perpendicular component of the applied magnetic field, $B\sin\theta$, of the magnetoresistance[18,22]. Therefore, to extract the pure 2D surface state contribution, we can subtract the 3D WAL contribution from the magnetoconductance at other angles, i.e. $\Delta G_{xx}(\theta,B) = 1/R_{xx}(\theta,B) - 1/R_{xx}(0,B)$. Fig. 4a shows traces of the sheet magnetoconductance as a function of $B\sin\theta$. $\Delta G_{xx}(\theta, B)$ displays cusp-like maxima at B=0 at each tilt angle and all traces follow the same
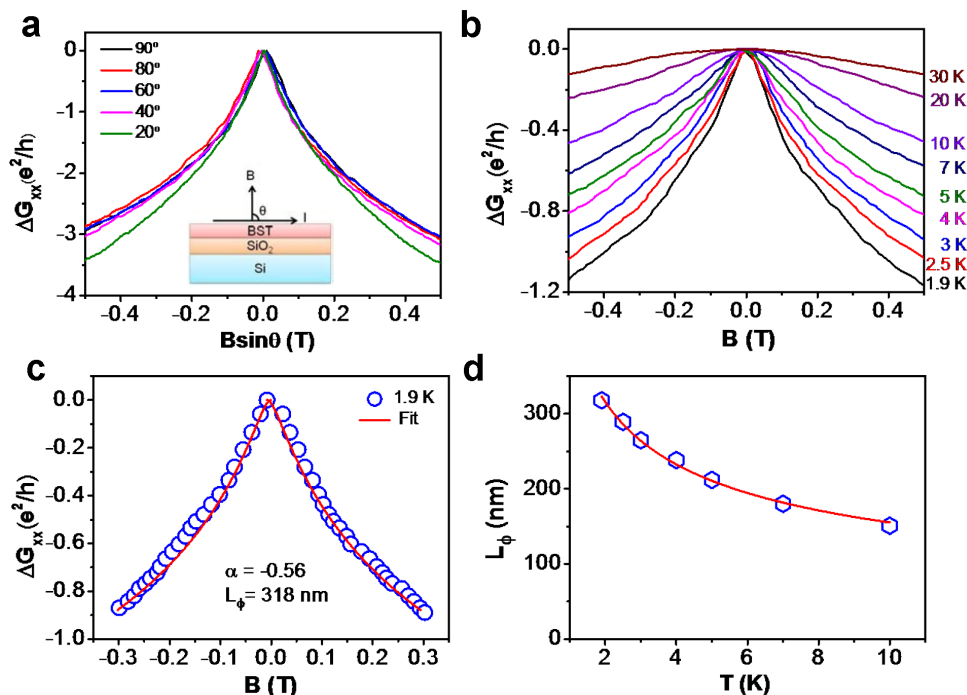
Figure 4 | Weak anti-localization (WAL) effect in BST crystal. (a) The change of sheet magnetoconductance plotted in the perpendicular magnetic field component of the magnetic field, Bsinθ, at 1.9 K. The only perpendicular component dependent features indicate that WAL is induced by 2D surface electrons. (b) The change of sheet magnetoconductance (ΔG_{xx}) in perpendicular magnetic fields (θ =90°) at temperatures ranging from 1.9 to 30 K. It shows the WAL features (sharp cusps at around zero magnetic field) persistent until 10 K. (c) Trace of sheet magnetoconductance's change at 1.9 K, the solid lines (red) are fits of 2D localization theory, where α is -0.56, and l_ϕ is 318 nm, confirming the 2D nature of WAL. (d) Temperature dependence of phase coherent length L_ϕ obtained by fitting ΔG_{xx} to 2D localization theory. The solid line (red) shows the power law dependence of temperature as $l_\phi \sim T^{-0.44}$.

curve at low magnetic fields (≤ 0.1 T) but they deviate from each other at higher magnetic fields, which confirms the 2D nature of WAL effect[18,22]. The temperature-dependent of ΔG_{xx} is shown in Fig. 4b, revealing the sharp negative cusps characteristic of WAL. Similar to previous observations[18,22,48], as the temperature increases, the cusps are broadened and finally disappear owing to the decrease in the phase coherent length at higher temperatures (Fig. 4d). The WAL can persist up to 10 K.

The quantum correction to the 2D magnetoconduction can be described by the Hikami-Larkin-Nagaoka (HLN) model[50]. In a strong spin-orbit interaction and a low mobility regime, i.e. $\tau_\phi \ll \tau_{SO}$ and $\tau_\phi \ll \tau_e$, the conduction correction is given by $\delta G_{WAL}(B) \equiv G(B) - G(0) \cong \alpha \frac{e^2}{2\pi^2\hbar}\left[\Psi\left(\frac{1}{2} + \frac{B_\phi}{B}\right) - \ln\left(\frac{B_\phi}{B}\right)\right]$, where τ_ϕ is dephasing time, $\tau_{SO}(\tau_e)$ is spin-orbit (elastic) scattering time, α is a WAL coefficient, e is the electronic charge, $\hbar$ is the reduced Planck's constant, Ψ is the digamma function, and $B_\phi = \hbar/4el_\phi^2$ is a magnetic field characterized by coherence length l_ϕ ($l_\phi = \sqrt{D\tau_\phi}$, D is diffusion constant). For the topological surface states the WAL should give α a value of -0.5[13,18,22,48,49]. Fitting ΔG_{xx} at 1.9 K with the HLN equation yields $\alpha = -0.56$ and $l_\phi = 318$ nm (Fig. 4c), confirming the 2D nature of WAL. The obtained coherence length as a function of temperature is shown in Fig. 4d. The coherence length decreases from 318 to 150 nm as the temperature increases from 1.9 to 10 K and this monotonous reduction of coherence length was also observed in other TI systems[22,48]. A power law fit of l_ϕ with temperature gives a relationship of $l_\phi \sim T^{-0.44}$ (Fig. 4d). Theoretically, for 2D systems the power law dependence of coherence length is $l_\phi \sim T^{-1/2}$, while for 3D system the power law dependence changes to be $l_\phi \sim T^{-3/4}$ (ref. 51). Hence, the temperature-dependent behavior of coherence length further proves that the WAL at low magnetic fields originated from the 2D surface states.

Quantum oscillations in BST crystal. Quantum oscillations such as SdH oscillations and Aharonov-Bohm (A-B) interference have been identified as convincing tools for characterizing surface states in topological insulators[12,19,34,35,52]. Compared with extensive exploration of SdH oscillations in Bi_2Te_2Se (BTS)[14,38] and in Sn-doped BTS crystal[20], surface transport properties were rarely investigated in its "sister" tetradymite structure-Bi_2Se_2Te (BST) crystal although theoretical calculations predicted it to be an excellent TI candidate[25]. In this regard, we carried out low-temperature magnetotransport measurements to provide experimental evidence for the surface state dominated transport in BST crystal. The magnetic field is perpendicular to both the current flow and the surface of the BST nanoflake. The magnetic-field dependent longitudinal resistance R_{xx} shows traces of SdH oscillations in our raw data (Supplementary Fig. S5a). After a direct subtraction of the smooth background (Supplementary Fig. S5a), the oscillatory part of R_{xx} (ΔR_{xx}) displays periodic peaks (maxima) and valleys (minima) with 1/B (Fig. 5a), revealing the evident existence of a well-defined Fermi surface[12,34,53]. The SdH oscillations survive up to 7 K (Fig. 5a). A single oscillation frequency can be extracted from fast Fourier transform (FFT) spectra ($f_{SdH}(T) \sim 44.9$ T, Supplementary Fig. S6). For a 2D system, the SdH oscillation frequency is directly related to the cross section A_F of the Fermi surface in momentum space via the Onsager relation: $f_{SdH} = \left(\frac{h}{4\pi^2 e}\right)A_F$, where $A_F = \pi k_F^2$, k_F is the Fermi vector, e is the electron charge, and h is Planck constant. The 2D surface carrier density n_{2D} is related to k_F by $n_{2D} = k_F^2/4\pi$. By substituting f_{SdH}, the Fermi vector k_F can be determined to be 0.037 Å^{-1}, corresponding to a 2D carrier density of 1.1×10^{12} cm^{-2}. If the SdH oscillations come from the bulk state, the period of SdH oscillations must be related to a 3D Fermi sphere with a radius of $k_F = 0.037$ Å^{-1} in momentum space and give a carrier density of 7.45×10^{18} cm^{-3}, which is completely inconsistent with the Hall value of
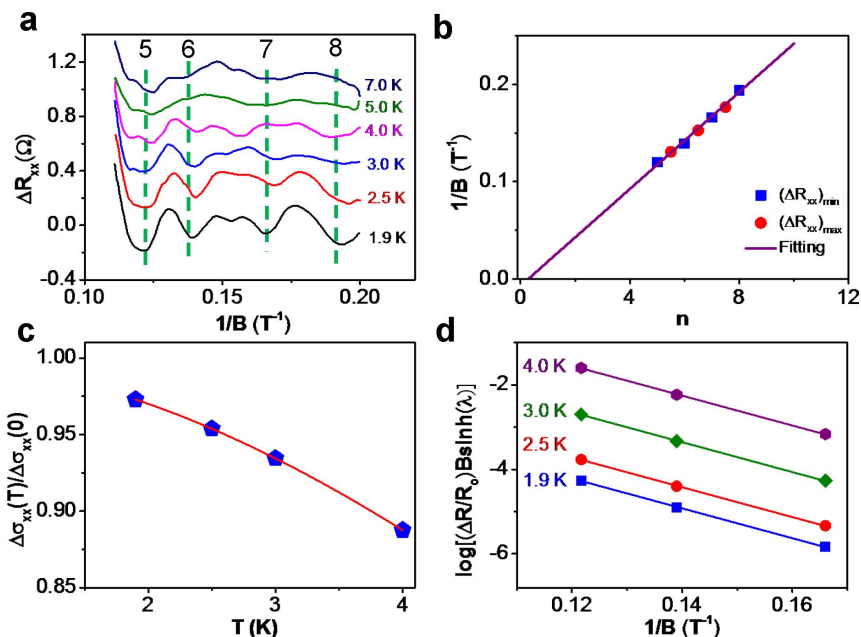
Figure 5 | SdH oscillations in BST crystal. (a) Shubnikuv-de Hass oscillations at different temperatures. The green dashed lines mark the SdH dips at Laudau filling factors of 5, 6, 7, and 8. (b) Landau-level fan diagram for SdH oscillations in ΔR_{xx}. Linear fitting of the periodic maxima and minima as a function of the Landau level index n gives a nonzero intersects of 0.29, corresponding to a nonzero Berry's phase of 0.42π. (c) Temperature dependence of the normalized conductivity amplitude $\Delta\sigma_{xx}(T)/\Delta\sigma_{xx}(0)$. The solid line (red) is best fit to $\lambda(T)/\sinh(\lambda(T))$. A magnetic field of 7.6 T was used to extract the cyclotron effective mass: $\sim 0.111 m_0$. (d) Dingle plots of log $[(\Delta R/R_0)B\sinh(\lambda)]$ versus 1/B at four different temperatures. Transport lifetime τ, mean free path $\ell = V_F\tau$, and mobility μ can be extracted from the best fit to log $[(\Delta R/R_0)B\sinh(\lambda)]$.

1.4×10^{16} cm^{-3}. Thus, the SdH oscillations are originated from 2D surface states. In Fig. 5b, we plot the 1/B values corresponding to the maxima (red closed circles) and the minima (blue closed rectangles) of ΔR_{xx} versus Landau level index n by assigning the index in the regime of Ref.19. Linear fitting of the data yields a finite intercept of 0.29 (corresponding to a Berry phase of 0.42π), highlighting the topological surface states as the origin of the SdH oscillations. The discrepancy of the extrapolated values with the expected value of 0.5 from the massless Dirac fermions were reported by several groups[14,19,20,34,38] and the possible origin of this discrepancy is attributed to the Zeeman coupling of the spin to the magnetic field[19,49], in which a 2D quantum limit was achieved under a high magnetic field (~ 60 T)[19]. Another possible explanation of the discrepancy is attributed to the deviation of dispersion relation from an ideal linear dispersion for Dirac fermions[36,54]. In the present study, the magnetoresistance measurement was performed at a much lower magnetic field (9 T), therefore we believe that this discrepancy arises from the non-ideal linear dispersion in the energy bands[54], which is also shown in the ARPES spectrum of BST (Fig. 2). In addition, the fitting of 1/B (minima and maxima of ΔR_{xx}) with Landau filling level n can also give a value of $k_F = 0.036$ Å^{-1}, which is in a good agreement with the aforementioned SdH calculations.

The temperature-dependent amplitude of $\Delta\sigma_{xx}$ of the SdH oscillations can be described by $\Delta\sigma_{xx}(T)/\Delta\sigma_{xx}(0) = \lambda(T)/\sinh(\lambda(T))$, where $\lambda(T) = 2\pi^2 k_B T m_{cycl}/(\hbar eB)$, m_{cycl} is the cyclotron mass, $\hbar$ is the reduced Planck's constant, and k_B is Boltzmann's constant. By performing the best fit of the conductivity oscillation amplitude to

the $\Delta\sigma_{xx}(T)/\Delta\sigma_{xx}(0)$ equation, m_{cycl} is extracted to be ~ 0.111 m_e (m_e is the free electron mass), as shown in Fig. 5c. The Fermi level is described by $E_F = m_{cycl}V_F^2$ and V_F is related to k_F by $m_{cycl}V_F = \hbar k_F$, where V_F is the Fermi velocity[12,34,55]. This yields a Fermi level of ~ 95 meV above the Dirac point and a Fermi velocity of 3.9×10^5 m s^{-1}, which are smaller than those from the ARPES results. Previous reports on Bi$_2$Se$_3$ suggests that for samples with low carrier concentration ($\sim 10^{17}$ cm^{-3}), discrepancies emerge for the position of the Fermi level inferred from ARPES and from transport experiments[55]. Surface charge accumulation induced band-bending is responsible for the discrepancy[19,55], while the lower Fermi velocity (3.9×10^5 m s^{-1}) obtained from SdH oscillations compared with that of ARPES (6.4×10^5 m s^{-1}) is probably due to the deviations of surface states from the linear dispersion when going away from the Dirac point[42].

The transport lifetime of the surface states (τ) can be estimated by utilizing the Dingle plot[12,19,34,52]. Since $\Delta R/R_0 \sim [\lambda(T)/\sinh\lambda(T)]e^{-D}$, where $D = 2\pi^2 E_F/\tau e B V_F^2$, the lifetime τ can be derived from the slope in Dingle plot by $\log[(\Delta R/R_0)B\sinh(\lambda(T))]\approx[2\pi^2 E_F/(\tau e V_F^2)]\times(1/B).(\tau e V_F^2)]\times(1/B)$ (Fig. 4d). The fit in Fig. 4d gives a transport lifetime of $\sim 3.5\times10^{-13}$ s, corresponding to a mean free path ℓ of ~ 136 nm ($\ell = V_F\tau$). The surface mobility $\mu_s = e\tau/m_{cycl} = e\ell/\hbar k_F$ can be estimated as ~ 5593 cm^2 V^{-1} s^{-1}, which is more than twenty times larger than the Hall mobility of 264 cm^2 V^{-1} s^{-1} from the bulk (see Table 1). According to these calculated results, the surface contribution to the total conduction can be estimated as $\sim 57\%$ (see Table 2), which suggests dominant surface transport in BST crystal.

Table 1 | Estimated parameters from the SdH oscillations at T = 1.9 K

f_{SdH} (T)	N_{2D} (10^{12} cm^{-2})	m_{cycl} (m$_0$)	k_F (Å^{-1})	V_F (10^5 ms^{-1})	E_F (meV)	τ (10^{-13} s)	ℓ (nm)	μ (cm^{2}V^{-1}s^{-1})
44.9	1.1	0.111	0.037	3.9	~95	3.53	~136	~5593

Table 2 | Estimated surface conduction contribution with zero magnetic field at T= 1.9 K

G (surface) (mS)	R (total) (Ω)	R_{sheet} (total) (ΩW^{-1})	G_{sheet} (total) (mS)	G (surface)/ G_{sheet} (total)
1.97	412.7	289.3	3.46	~57%

Discussion

In summary, ARPES experiments provide direct evidence of topological surface states in the BST crystal. The high binding energy of the Dirac point probably originates from the Se vacancies created by Se out-diffusion[56] during the pre-annealing process prior to ARPES measurements. In addition, the non-stoichiometric form of BST ($Bi_2Se_{1.88}Te_{1.12}$) can be considered as excessive substitution of Se atoms in outmost quintuple layers of Bi_2Se_3 by Te atoms, which effectively compensates the Se vacancies and lift up the position of the conduction band minimum, leading to the absence of the conduction band in full photon energy-dependent ARPES measurement (Fig. 2)[25,40,42]. Both the WAL effect and SdH oscillations have unambiguously shown dominate surface transport in the BST crystal. Theoretical calculations predict that introducing Te into the central layer of Bi_2Se_3 to form the ordered BST structure may make it a superior TI material that behaves like Bi_2Se_3 with a well-defined Dirac cone located inside the bulk band gap[25]. However, finding effective ways of introducing Te into the central layer remains a challenge. Doping BST further with compensation elements, like Sb[24] and Sn[20], may provide an alternative way for tuning the relative position of Fermi level and Dirac point, making the BST crystal an ideal platform for exploring exotic quantum physical phenomena and device applications.

Methods

Sample preparation and characterization. High-quality single crystalline Bi_2Se_2Te (BST) with a small concentration gradient was obtained by the Bridgman technique. Proper ratios of high purity metals of bismuth (99.999%), selenium (99.999%) and tellurium (99.999%) were sealed in a quartz tube and melted into an ingot in an induction furnace to homogenize the composition. The ingot was then sealed in a quartz tube with a larger diameter and loaded into a Bridgman furnace. A crystal was obtained by withdrawing the quartz tube at 1 mm/hr after being heated to 800°C and kept at a constant temperature. Concentration profiles along the ingot were obtained by using electron probe micro-analysis which was performed in a JEOL JAMP-7830F Auger Microprobe. (Supplementary information). Thin flakes of BST with typical sizes of several micrometers in length/width were mechanically exfoliated from bulk crystals and transferred onto holey carbon copper grids for TEM characterizations, which were performed with a FEI Tecnai F20 TEM operating at 200 KV and equipped with an energy-dispersive spectroscopy detector.

Angle-resolved photoemission spectroscopy experiments. High-resolution ARPES experiments were performed on beam line 12.0.1 of the Advance Light Source at Lawrence Berkeley National Laboratory. The data were recorded with a VG-Scienta SES100 electron analyzer at low temperature ($<$ 50 K) at photon energies ranging from 30 to 80 eV. The typical energy and momentum resolution was 20–30 meV and 1% of the surface Brillouin zone (BZ), respectively. Samples were cleaved in situ and were measured under a vacuum level better than 5×10^{-11} Torr.

Transport properties of BST. For transport measurements, Ohmic contacts were made by using room-temperature cured silver paste. The sample used for Hall measurements and SdH studies was 0.5 mm wide and 0.05 mm thick and the voltage contact distance is 0.6 mm. The longitudinal resistance R_{xx} and the transverse resistance R_{xy} were measured simultaneously by a standard six-probe method in a Quantum Design physical properties measurement system (PPMS-9T) which has a capability of sweeping the magnetic field between ± 9 T at temperatures down to 1.9 K.

1. Qi, X.-L. & Zhang, S.-C. Topological insulators and superconductors. *Rev. Mod. Phys.* **83**(4), 1057–1110 (2011).
2. Hasan, M. Z. & Kane, C. L. Colloquium: Topological insulators. *Rev. Mod. Phys.* **82**(4), 3045–3067 (2010).
3. Moore, J. TOPOLOGICAL INSULATORS The next generation. *Nat. Phys.* **5**(6), 378–380 (2009).
4. Hasan, M. Z. & Moore, J. E. Three-Dimensional Topological Insulators in *Annual Review of Condensed Matter Physics*, edited by J. S. Langer (2011), Vol. 2, pp. 55–78.
5. Bernevig, B. A., Hughes, T. L. & Zhang, S. C. Quantum spin Hall effect and topological phase transition in HgTe quantum wells. *Science* **314**, 1757–1761 (2006).
6. Koenig, M. *et al.* Quantum spin hall insulator state in HgTe quantum wells. *Science* **318**(5851), 766–770 (2007).
7. Zhang, H. *et al.* Topological insulators in Bi_2Se_3, Bi_2Te_3 and Sb_2Te_3 with a single Dirac cone on the surface. *Nat. Phys.* **5**(6), 438–442 (2009).
8. Fu, L. & Kane, C. L. Superconducting proximity effect and Majorana fermions at the surface of a topological insulator. *Phys. Rev. Lett.* **100**(9) (2008).
9. Qi, X.-L., Li, R., Zang, J. & Zhang, S.-C. Inducing a magnetic monopole with topological surface states. *Science* **323**(5918), 1184–1187 (2009).
10. Stanescu, T. D., Sau, J. D., Lutchyn, R. M., & Das Sarma, S. Proximity effect at the superconductor-topological insulator interface. *Phys. Rev. B* **81**(24) (2010).
11. Moore, J. E. The birth of topological insulators. *Nature* **464**(7286), 194–198 (2010).
12. Xiu, F. *et al.* Manipulating surface states in topological insulator nanoribbons. *Nat. Nanotech.* **6**(4), 216–221 (2011).
13. Chen, J. *et al.* Gate-voltage control of chemical potential and weak antilocalization in Bi_2Se_3. *Phys. Rev. Lett.* **105**(17), 176602 (2010).
14. Ren, Z., Taskin, A. A., Sasaki, S., Segawa, K. & Ando, Y. Large bulk resistivity and surface quantum oscillations in the topological insulator Bi_2Te_2Se. *Phys. Rev. B* **82**(24), 243106 (2010).
15. Checkelsky, J. G., Hor, Y. S., Cava, R. J. & Ong, N. P. Bulk band gap and surface state conduction observed in voltage-tuned crystals of the topological insulator Bi_2Se_3. *Phys. Rev. Lett.* **106**(19), 196801 (2011).
16. Hong, S. S., Cha, J. J., Kong, D. & Cui, Y. Ultra-low carrier concentration and surface-dominant transport in antimony-doped Bi_2Se_3 topological insulator nanoribbons. *Nat. Communi.* **3**, 757 (2012).
17. Chen, Y. L. *et al.* Massive Dirac fermion on the surface of a magnetically doped topological insulator. *Science* **329**(5992), 659–662 (2010).
18. He, H.-T. *et al.* Impurity effect on weak antilocalization in the topological insulator Bi_2Te_3. *Phys. Rev. Lett.* **106**(16), 166805 (2011).
19. Analytis, J. G. *et al.* Two-dimensional surface state in the quantum limit of a topological insulator. *Nat. Phys.* **6**(12), 960–964 (2010).
20. Ren, Z., Taskin, A. A., Sasaki, S., Segawa, K. & Ando, Y. Fermi level tuning and a large activation gap achieved in the topological insulator Bi_2Te_2Se by Sn doping. *Phys. Rev. B* **85**(15), 155301 (2012).
21. Kong, D. *et al.* Ambipolar field effect in the ternary topological insulator $(Bi_xSb_{1-x})_2Te_3$ by composition tuning. *Nat. Nanotech.* **6**(11), 705–709 (2011).
22. Cha, J. J. *et al.* Weak antilocalization in $Bi_2(Se_xTe_{1-x})_3$ nanoribbons and nanoplates. *Nano Letters* **12**(2), 1107–1111 (2012).
23. Zhang, J. *et al.* Band structure engineering in $(Bi_{1-x}Sb_x)_2Te_3$ ternary topological insulators. *Nat. Communi.* **2**, 574 (2011).
24. Arakane, T. *et al.* Tunable Dirac cone in the topological insulator $Bi_{2-x}Sb_xTe_{3-y}Se_y$. *Nat. Communi.* **3**, 636 (2012).
25. Wang, L.-L. & Johnson, D. D. Ternary tetradymite compounds as topological insulators. *Phys. Rev. B* **83**(24), 241309 (2011).
26. Hsieh, D. *et al.* A topological Dirac insulator in a quantum spin Hall phase. *Nature* **452**(7190), 970–974 (2008).
27. Chen, Y. L. *et al.* Experimental realization of a three-dimensional topological insulator, Bi_2Te_3. *Science* **325**(5937), 178–181 (2009).
28. Hsieh, D. *et al.* Observation of time-reversal-protected single-Dirac-cone topological-insulator states in Bi_2Te_3 and Sb_2Te_3. *Phys. Rev. Lett.* **103**(14), 146401 (2009).
29. Xia, Y. *et al.* Observation of a large-gap topological-insulator class with a single Dirac cone on the surface. *Nat. Phys.* **5**(6), 398–402 (2009).
30. Zhang, Y. *et al.* Crossover of the three-dimensional topological insulator Bi_2Se_3 to the two-dimensional limit. *Nat. Phys.* **6**(8), 584–588 (2010).
31. Roushan, P. *et al.* Topological surface states protected from backscattering by chiral spin texture. *Nature* **460**(7259), 1106–1109 (2009).
32. Zhang, T. *et al.* Experimental demonstration of topological surface states protected by time-reversal symmetry. *Phys. Rev. Lett.* **103**(26), 266803 (2009).
33. Hanaguri, T., Igarashi, K., Kawamura, M., Takagi, H. & Sasagawa, T. Momentum-resolved Landau-level spectroscopy of Dirac surface state in Bi_2Se_3. *Phys. Rev. B* **82**(8), 081305 (2010).
34. Qu, D.-X., Hor, Y. S., Xiong, J., Cava, R. J. & Ong, N. P. Quantum oscillations and Hall anomaly of surface states in the topological insulator Bi_2Te_3. *Science* **329**(5993), 821–824 (2010).
35. Peng, H. *et al.* Aharonov-Bohm interference in topological insulator nanoribbons. *Nat. Mater.* **9**(3), 225–229 (2010).
36. Taskin, A. A., Ren, Z., Sasaki, S., Segawa, K., & Ando, Y. Observation of Dirac holes and electrons in a topological insulator. *Phys. Rev. Lett.* **107**(1), 016801 (2011).

37. McIver, J. W., Hsieh, D., Steinberg, H., Jarillo-Herrero, P. & Gedik, N. Control over topological insulator photocurrents with light polarization. *Nat. Nanotech.* **7**(2), 96–100 (2012).

38. Xiong, J. *et al.* Quantum oscillations in a topological insulator Bi_2Te_2Se with large bulk resistivity (6 Ω cm). *Physica E* **44**(5), 917–920 (2012).

39. Bindi, L. & Cipriani, C. The crystal structure of skippenite, Bi_2Se_2Te, from the Kochkar deposit, southern Urals, Russian Federation. *Can. Mineral.* **42**, 835–840 (2004).

40. Jia, S. *et al.* Low-carrier-concentration crystals of the topological insulator Bi_2Te_2Se. *Phys. Rev. B* **84**(23), 235206 (2011).

41. Nakajima, S. Crystal Structure of $Bi_2Te_{3-x}Se_x$ *J. Phys. Chem. Solids* **24**(3), 479–485 (1963).

42. Miyamoto, K. *et al.* Topological surface states with presistent high spin polarization across Dirac point in Bi_2Te_2Se and Bi_2Se_2Te. *arXiv, 1203.4439v1* (2012).

43. Scanlon, D. O. *et al.* Controlling bulk conductivity in topological insulators: Key role of anti-Site defects. *Adv. Mater.* **24**(16), 2154–2158 (2012).

44. Shklovskii, B. I. & Efros, A. L. *Electronic Properties of Doped Semiconductors.* (Springer-Verleg, Berlin, 1984).

45. Mott, N. F. Conduction in non-crystalline materials .3. Localized states in a pseudogap and near extremities of conduction and valence bands. *Philos. Mag.* **19**(160), 835–852 (1969).

46. Steinberg, H. Laloe, J. B., Fatemi, V., Moodera, J. S., & Jarillo-Herrero, P. Electrically tunable surface-to-bulk coherent coupling in topological insulator thin films. *Phys. Rev. B* **84**(23), 233101 (2011).

47. Liu, M. *et al.* Crossover between weak antilocalization and weak localization in a magnetically doped topological insulator. *Phys. Rev. Lett.* **108**(3), 036805 (2012).

48. Matsuo, S. *et al.* Weak antilocalization and conductance fluctuation in a submicrometer-sized wire of epitaxial Bi_2Se_3. *Phys. Rev. B* **85**(7), 075440 (2012).

49. Chen, J. *et al.* Tunable surface conductivity in Bi_2Se_3 revealed in diffusive electron transport. *Phys. Rev. B* **83**(24), 241304 (2011).

50. Hikami, S., Larkin, A. I. & Nagaoka, Y. Spin-orbit interaction and magnetoresistance in the two dimensional random system *Prog. Theor. Phys.* **63**(2), 707–710 (1980).

51. Altshuler, B. L., Aronov, A. G. & Khmelnitsky, D. E. Effects of electron-electron collisons with small energy transfers on quantum localization. *J. Phys. C* **15**(36), 7367–7386 (1982).

52. Taskin, A. A. & Ando, Y. Quantum oscillations in a topological insulator $Bi_{1-x}Sb_x$. *Phys. Rev. B* **80**(8), 085303 (2009).

53. Eto, K., Ren, Z., Taskin, A. A., Segawa, K. & Ando, Y. Angular-dependent oscillations of the magnetoresistance in Bi_2Se_3 due to the three-dimensional bulk Fermi surface. *Phys. Rev. B* **81**(19) (2010).

54. Taskin, A. A. & Ando, Y. Berry phase of nonideal Dirac fermions in topological insulators. *Phys. Rev. B* **84**(3), 035301 (2011).

55. Analytis, J. G. *et al.* Bulk Fermi surface coexistence with Dirac surface state in Bi_2Se_3: A comparison of photoemission and Shubnikov-de Haas measurements. *Phys. Rev. B* **81**(20), 205407 (2010).

56. Kim, Y. S. *et al.* Thickness-dependent bulk properties and weak antilocalization effect in topological insulator Bi_2Se_3. *Phys. Rev. B* **84**(7), 073109 (2011).

Acknowledgements

Author contributions

F. X. conceived the idea and supervised the overall research. L. Bao and L. H. designed and performed the experiments. L. H. fabricated the devices and carried out low-temperature transport measurements. T. R. and T. L. synthesized the Bi_2Se_2Te crystal. Z. C. and J. Z. performed the structural analysis. P. Z. and A. V. carried out the ARPES measurements. N. M. and L. H contributed to the analysis. L. Bao, N. M. and F. X., wrote the paper with helps from all other co-authors. L. Bao and L. H. contributed equally to this work.

Additional information

How to cite this article: Bao, L. *et al.* Weak Anti-localization and Quantum Oscillations of Surface States in Topological Insulator Bi_2Se_2Te. *Sci. Rep.* **2**, 726; DOI:10.1038/srep00726 (2012).